

Directional miscentering dependence in weak lensing mass bias

Martin W. Sommer^{1*}, Tim Schrabback^{1,2}, and Sebastian Grandis²,

¹*Argelander-Institut für Astronomie, Auf dem Hügel 71, D-53121 Bonn, Germany*

²*Universität Innsbruck, Institut für Astro- und Teilchenphysik, Technikerstr. 25/8, 6020 Innsbruck, Austria*

(MNRAS submitted)

ABSTRACT

Galaxy cluster masses estimated from parametric modeling of weak lensing shear observations are known to be biased by inaccuracies in observationally determined centers. It has recently been shown that such systematic effects can be non-isotropic when centers are derived from X-ray or Compton-Y (Sunyaev-Zeldovich effect) observations, which is often the case in practice. This fact challenges current methods of accurately correcting for weak lensing mass biases using simulations paired with isotropic empirical miscentering distributions, in particular as the effect on determined masses is currently a dominant source of systematic uncertainty. We use hydrodynamical cosmological simulations taken from the Magneticum Pathfinder simulations to show that the non-isotropic component of the mass bias can be reduced to within one percent of the mass when considering the center of mass, rather than the bottom of the gravitational potential, as the reference center of a galaxy cluster.

Key words: gravitational lensing: weak – galaxies: clusters: general

1 INTRODUCTION

The distribution of clusters of galaxies, or halos, throughout the Universe traces the evolution of the matter distribution through space and time. In particular, the number density of galaxy clusters as a function of redshift and mass — what is called the halo mass function — depends critically upon the curvature of the Universe and the growth rate of primordial density fluctuations (e.g. Haiman et al. 2001), and thereby provide ways to investigate numerous aspects of the standard model of cosmology (e.g. Allen et al. 2011; Bocquet et al. 2024; Ghirardini et al. 2024). As masses are often inferred from mass-observable relations, the latter must in turn be calibrated through more direct means of measuring mass.

The mass of a galaxy cluster is not uniquely defined, in part because the concept of a halo in itself has no strict definition. In the context of cosmology, a mass definition that can be exactly replicated in models and simulations is desirable. For this reason, the cluster mass is typically defined as the total mass inside a spherical region, defined such that the mean matter density inside this region is some overdensity factor Δ higher than either the critical or the mean mass density of the universe at the redshift of the halo. A mass M_Δ determined in this way then corresponds directly to a radius r_Δ , given a suitably chosen center of the cluster. The choice of definition for said center coordinate, the accuracy with which it can be determined in observations, and systematic biases occurring from the lack of such accuracy are the central topics of investigation in this work.

In modeling the halo mass function, a long-standing practice has been to use the bottom of the gravitational potential well of the halo as the center coordinate, in particular as this choice conforms to models of spherical infall (Press & Schechter 1974; Bond et al. 1991). While such models were initially shown to be remarkably consistent with

early n-body simulations (Jenkins et al. 2001), more accurate models were later developed based on fits to simulations over large ranges of redshifts (e.g. Sheth & Tormen 1999; Springel et al. 2005b). In more recent years, a process called mass function emulation, by which numerical simulations with varying parameters of the cosmological model are sampled, has been developed and refined (e.g. Heitmann et al. 2006; Bocquet et al. 2020). Given that the computation of the mass function at present is almost exclusively based on simulations, the definition of the halo center can be modified, as long as it can be uniquely defined from the mass distribution of a halo.

Because all mass acts gravitationally, arguably the most direct way of determining the mass of a halo observationally is through the distortion of background sources (galaxies) by its gravitational potential — the effect known as weak gravitational lensing (henceforth WL). There is a multitude of studies calibrating mass-observable relations in this way (e.g. Applegate et al. 2014; Mantz et al. 2014; Planck Collaboration 2016; Schrabback et al. 2018; Dietrich et al. 2019; Bocquet et al. 2019; McClintock et al. 2019; Schrabback et al. 2021; Zohren et al. 2022; Grandis et al. 2024). WL masses, in turn, suffer from a variety of systematic biases that must be corrected for, a problem that is receiving increasing attention as statistical uncertainties continue to decrease (e.g. Grandis et al. 2019).

In this work, we are concerned with systematics pertaining to the accuracy of the weak lensing mass modeling, that is, we assume the data themselves are free of bias. We also neglect the effects of projection of uncorrelated matter along the line of sight (Hoekstra et al. 2011) and triaxiality (e.g. Applegate et al. 2016; Dietrich et al. 2019), and the impact of parametric models of mass density (although we do use such a model). Our concern is purely with miscentering, that is, the impact of the choice of coordinates around which a specific azimuthally symmetric density model is taken.

Significant efforts have been made towards quantifying the distribution of weak lensing mass bias distributions from simulations

* E-mail: mnord@astro.uni-bonn.de (MWS)

(Becker & Kravtsov 2011; Oguri & Hamana 2011; Bahé et al. 2012; Henson et al. 2017; Lee et al. 2018), mostly considering cases in which no miscentering is present. More recent studies, accounting for miscentering effects (e.g. Dietrich et al. 2019; Schrabback et al. 2021; Grandis et al. 2021; Zohren et al. 2022; Chiu et al. 2023), report estimates of residual systematic uncertainties on mass modeling bias between one and several percent, albeit without explicitly accounting for the possibility an anisotropic miscentering distribution. Sommer et al. (2024, henceforth S+24) recently found that such effects may induce systematic errors of several percent using center coordinates derived either from peaks in the Compton-Y distortion (Sunyaev-Zeldovich effect, also SZE, Sunyaev & Zeldovich 1970, 1980) or centroids in the X-ray brightness – both fairly standard approaches in practice (e.g. Schrabback et al. 2021; Bocquet et al. 2023; Kleinebreil et al. 2024).

In this work, we shift the focus away from the observed cluster center, and towards the reference position; that is, the definition of the halo center. In particular, we explore the possibility of taking the center of mass, rather than the bottom of the gravitational potential, as the reference. Through simulations, we investigate whether non-isotropic effects in the weak lensing mass bias can be reduced to a level below or similar to the expected statistical mass uncertainties of ongoing and planned large scale surveys.

In Section 2 we cover the necessary definitions for weak lensing observables and describe how lensing and SZE images are extracted from the simulated sample. The processes of generating and randomizing miscentering distributions for the study of anisotropies in the weak lensing mass bias are described, as well as the determination of halo mass given various center coordinates. We report our results in Section 3, discuss their implications and limitations in Section 4, and offer our conclusions in Section 5.

We use the flat Λ CDM cosmological model of Komatsu et al. (2011), with Hubble parameter $h = 0.704$ and total mass density $\Omega_m = 0.272$. Mass is quantified in terms of $\Delta = 500$, where Δ is the overdensity with respect to the critical density of the universe at the redshift of a galaxy cluster. We define the weak lensing mass bias as the ratio $b = \frac{M_{\text{WL}}}{M_{\text{true}}}$, where M_{WL} and M_{true} are the measured and true masses, respectively. The natural logarithm is denoted $\log()$.

2 METHOD

2.1 Shear and convergence

The distortion of a background source at redshift z_s by a foreground lens (here, a cluster of galaxies) at redshift z_l is described in terms of the convergence κ and the shear γ . The former is the surface mass density $\Sigma(\theta)$ in units of the critical density

$$\Sigma_{\text{crit}} = \frac{c^2}{4\pi G} \frac{1}{D_1\beta} \quad (1)$$

at projected position θ , where c is the speed of light, G is the gravitational constant and the lensing efficiency β is defined as

$$\beta = \frac{D_{ls}}{D_s} H(z_s - z_l), \quad (2)$$

with D_s , D_l , D_{ls} the angular diameter distances between observer and source, observer and lens, and lens and the source, respectively.¹ The Heaviside step function, $H(z_s - z_l)$, is equal to one when $z_s > z_l$,

¹ In the following, we shall take the positional argument θ as implicit.

and zero otherwise (reflecting the fact that lensing occurs only if the source is behind the lens).

Shape distortions can be characterized by the reduced shear $g = g_1 + ig_2$ through $g = \frac{\gamma}{1-\kappa}$, where γ is the (unobservable) complex shear $\gamma = \gamma_1 + i\gamma_2$ (for an in-depth account we refer to Kilbinger 2015). For $|g| \leq 1$, the reduced shear can be estimated from averaged observed ellipticities² $\epsilon = \epsilon_1 + i\epsilon_2$, as (Seitz & Schneider 1997)

$$\epsilon = \frac{\epsilon_s + g}{1 + g^* \epsilon_s}, \quad (3)$$

where g^* is the complex conjugate of the reduced shear, and ϵ_s is the intrinsic complex ellipticity of a source. Under the reasonable assumption that there are no preferred orientations among the sources, the expectation value of ϵ_s vanishes, so that the ellipticity is an unbiased estimator of the reduced shear.

Shear, reduced shear and ellipticity can be decomposed into tangential (subscript t) and cross (subscript x) components through

$$\begin{aligned} (\cdot)_t &= -(\cdot)_1 \cos(2\alpha) - (\cdot)_2 \sin(2\alpha) \\ (\cdot)_x &= +(\cdot)_1 \sin(2\alpha) - (\cdot)_2 \cos(2\alpha), \end{aligned} \quad (4)$$

where (\cdot) denotes any of g , γ and ϵ , and α is the azimuthal angle with respect to a chosen center.

While the cross shear term vanishes for any azimuthally symmetric mass distribution, the tangential shear can be expressed in terms of the surface mass density as (e.g. Kaiser et al. 1995; Wright & Brainerd 2000)

$$\gamma_t(r) = \frac{\bar{\Sigma}(< r) - \bar{\Sigma}(r)}{\Sigma_{\text{crit}}}, \quad (5)$$

where $\bar{\Sigma}(< r)$ is the mean surface mass density inside the projected radius r , and $\bar{\Sigma}(r)$ is the surface mass density at radius r .

2.2 Simulations

We make use of the box2b-hr simulation box from the Magneticum Pathfinder³ suit of simulations (Hirschmann et al. 2014; Teklu et al. 2015; Dolag et al. 2016), in particular the redshift slice at $z = 0.67$ (snapshot 22). The simulation, implemented with magnetohydrodynamics in the cosmological Smoothed Particle Hydrodynamics (SPH) code GADGET (Springel et al. 2001; Springel 2005), has a volume of $640^3 h^{-3} \text{Mpc}^3$ and 2×2880^3 particles, and accounts for cooling, star formation and winds (Springel & Hernquist 2003; Wiersma et al. 2009); metals, stellar populations and chemical enrichment (Tornatore et al. 2007); black holes and AGN feedback (Springel et al. 2005a; Fabjan et al. 2010); thermal conduction (Dolag et al. 2004); turbulence (Dolag et al. 2005b) and passive magnetic fields (Dolag & Stasyszyn 2009). The data products were obtained using the Magneticum web portal⁴, using the tools ClusterFind (Ragagnin et al. 2017) and SMAC (Dolag et al. 2005a).

Selecting the 275 most massive halos from the simulation box, the resulting mean and median M_{500} are $1.69 \times 10^{14} h^{-1} M_\odot$ and $1.45 \times 10^{14} h^{-1} M_\odot$, respectively. After projecting each target onto three mutually orthogonal planes, we extract SZE Compton-Y as well as projected mass images, taking into account simulation particles within $\pm 30 h^{-1} \text{Mpc}$ along the line of sight from the position of the most bound particle.

² We define ellipticity as $\epsilon = (a - b)/(a + b) \cdot e^{2i\phi}$ for elliptical isophotes with minor-to-major axis ratio b/a and position angle ϕ .

³ <http://www.magneticum.org/>

⁴ <https://c2pacosmosim.srv.lrz.de/>

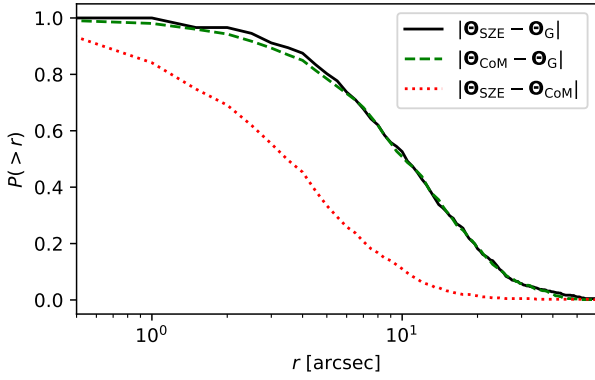


Figure 1. Azimuthally averaged miscentering distributions, shown as the estimated probability $P(> r)$ that the miscentering amplitude of a given target is greater than a radius r . The black solid line and the green dashed line show the miscentering of the SZE peak and the center of mass, respectively, from the gravitational center. The miscentering distribution of the SZE peak with respect to the center of mass is indicated by the red dotted line.

We derive the weak lensing shear and convergence, described in Section 2.1, from the projected mass at each pixel in the image, and set a constant lensing efficiency β . The latter has no direct bearing upon the results, as it only affects the noise level in derived masses.

To emulate the typical resolution of ground-based SZE observations, we convolve the SZE images with a two-dimensional Gaussian of one arcminute full width at half maximum. The peak of a thus convolved image is taken as the SZE center, Θ_{SZE} .

2.3 Miscentering

Starting from the position of the most bound particle, which we shall refer to as the gravitational center, or Θ_{G} , we derive the position of the center of mass, Θ_{CoM} , iteratively. The first estimate is the mass-weighted average position of all particles within a radius r_{500} from Θ_{G} . At each new position, we re-compute M_{500} and r_{500} from the local three-dimensional information on particle positions and masses using the SIMCUT⁵ tool (Ragagnin et al. 2017). Convergence (the projected difference between positions being less than one second of arc) is typically achieved within three iterations. Due to the recalibration of the center, we must distinguish the mass defined with respect to Θ_{CoM} , $M_{500, \text{CoM}}$, from the default mass $M_{500, \text{G}}$, defined in relation to the position Θ_{G} .

The SZE center Θ_{SZE} , which we shall use as an observational proxy, is the peak of the convolved SZE image as described in Section 2.2. S+24 devised an artificial broadening of the SZE miscentering distribution in order to approximately account for noise components due to primary anisotropies of the cosmic microwave background, millimeter emission from dusty galaxies, and noise from the instrument and Earth’s atmosphere. With respect to the issue of isotropic miscentering distributions, however, the latter work reports no significant difference using this broadened miscentering distribution. Thus, we work with noiseless SZE images here.

From the projected offsets between the centers defined above, we derive three azimuthally averaged empirical miscentering distributions, namely the distribution describing (i) the SZE peak position Θ_{SZE} with respect to the gravitational center Θ_{G} ; (ii) the center

of mass Θ_{CoM} with respect to Θ_{G} ; and finally (iii) Θ_{SZE} with respect to Θ_{CoM} . These distributions of projected miscentering offsets are shown in angular scale in Fig. 1. The miscentering distribution $|\Theta_{\text{SZE}} - \Theta_{\text{CoM}}|$ is considerably narrower than the two with Θ_{G} as reference (the latter two appearing very similar), suggesting a strong spatial correlation between the SZE peak and the center of mass.

In Fig. 2, we show the scatter between the SZE and center of mass miscenterings, indicating that the two are indeed strongly correlated. A different way to view the correlation is to separate the offsets between the SZE peak and the center of mass into orthogonal components, parallel and perpendicular to the direction of the center of mass (with respect to Θ_{G}).

In order to test whether miscentering distributions are isotropic, in the sense that the miscentering direction does not systematically alter the estimated weak lensing mass bias distribution, we randomize the distributions $|\Theta_{\text{SZE}} - \Theta_{\text{G}}|$, $|\Theta_{\text{SZE}} - \Theta_{\text{CoM}}|$ and $|\Theta_{\text{CoM}} - \Theta_{\text{G}}|$ by drawing (with replacement) for each halo a random absolute miscentering from the respective distribution, coupling it with a random angle $\varphi \in [0, 2\pi)$ in the sky plane. The process is schematically illustrated in Fig. 3. For clarity, we denote the thus randomized miscentering with a subscript (r).

2.4 Mass fitting

To estimate masses, we use the azimuthally symmetric Navarro-Frenk-White (NFW) density model (Navarro et al. 1997), which has shown reasonable consistency with galaxy clusters from both hydrodynamic (Tollet et al. 2016) and n-body (Bullock et al. 2001; Prada et al. 2012; Meneghetti et al. 2014; Klypin et al. 2016; Gupta et al. 2017) simulations. In the NFW model, the mass density $\rho(r)$ at physical radius R is given by

$$\rho(R) = \frac{M_{\Delta}}{4\pi f(c_{\Delta})} \frac{1}{R(R + \frac{r_{\Delta}}{c_{\Delta}})^2}, \quad (6)$$

where c_{Δ} is the so-called concentration parameter, and $f(c_{\Delta}) \equiv \log(1 + c_{\Delta}) - c_{\Delta}/(1 + c_{\Delta})$. Projecting the density onto the sky plane yields the mass surface density

$$\Sigma(r) = 2 \int_0^{\infty} \rho \left(\sqrt{r^2 + \zeta^2} \right) d\zeta, \quad (7)$$

where r is the projected radius from the chosen center, and ζ is in the direction of the line of sight. For the mass surface density and the resulting weak lensing shear, we make use of the analytical expressions derived by Bartelmann (1996).

We tie the concentration parameter c_{Δ} to the mass using the concentration-mass relation of Diemer & Kravtsov (2015), with the corrected parameters set of Diemer & Joyce (2019). While alternative choices of c_{Δ} strongly affect the normalization of the weak lensing mass bias distribution (e.g. Sommer et al. 2022), we do not expect a significant impact on the *difference* between two distributions derived using different centers.

We fit for the mass of each target using the projected density of Eq. (7) to predict the reduced tangential shear as a function of M_{500} , radially binning the reduced shear in the simulated images around each chosen center coordinate. In part due to the NFW model being somewhat unsuccessful in predicting the density near the halo center (e.g. Child et al. 2018), and in part to mitigate the effects of miscentering and magnification systematics, shear measurements with small radii are typically excised in weak lensing analyses (e.g. Henson et al. 2017). Here we fit to reduced shears with radii $r \in [r_{\text{min}}, r_{\text{max}}]$ from the center, with the inner radius $r_{\text{min}}=0.5$ Mpc and the outer radius $r_{\text{max}}=1.7$ Mpc. The latter value is chosen so as

⁵ <https://c2pacosmosim.srv.lrz.de/map/simcut>

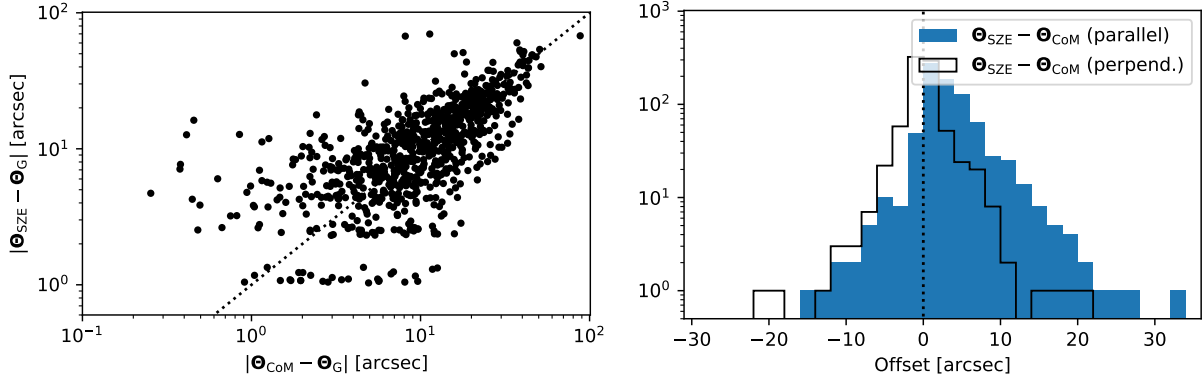


Figure 2. Left: projected center offsets of SZE peaks vs. centers of mass, both with respect to the gravitational center, for the 825 targets in the sample. The dotted line indicates the one-to-one-relation. Right: histogram of the projected offsets between Θ_{SZE} and Θ_{CoM} , decomposed into components respectively parallel and perpendicular to the vector $\Theta_{\text{CoM}} - \Theta_{\text{G}}$.

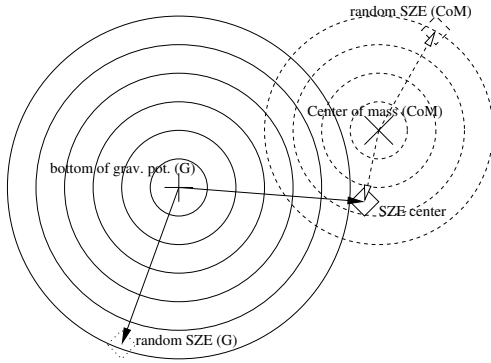


Figure 3. Schematic view of the miscentering distributions used in this work. Apart from the position of the SZE center taken as the peak SZE emission the simulations, random SZE centers are generated in two ways, namely from the distributions of $|\Theta_{\text{SZE}} - \Theta_{\text{G}}|$ and $|\Theta_{\text{SZE}} - \Theta_{\text{CoM}}|$.

to minimize both the two-halo term (e.g. Seljak 2000, Mandelbaum et al. 2005) and errors in the reduced shear — as shear is a non-local measure, any localized shear image will have large errors towards the outskirts of the image.

As the determination of the weak lensing mass bias has been found not to be sensitive to the level of statistical noise (Sommer et al. 2022), no noise is added to the reduced shear. Instead, the data are weighted to reflect the growth of radial bins with projected radius.

The weak lensing mass bias b is defined as the ratio of measured to reference ("true") mass, where the latter is either $M_{500,G}$ or $M_{500,CoM}$ (Section 2.3). The choice of reference mass is not contingent upon the choice of reference center; we are free to define the center coordinate and the reference mass independently of one another.

For each centering convention applied to our sample, we model the distribution of b with normal and log-normal distributions. While neither perfectly models the mass bias, S+24 found that either one can provide a reasonable approximation. We use the symbols (μ_b, σ_b) to respectively mean the estimated mean and standard deviation in linear space, and similarly $(\mu_{\log b}, \sigma_{\log b})$ for the log-normal case.

Given an estimate of the mass bias distribution, a measured mass can be corrected, dividing by random samples from the former and propagating the uncertainties of the measurements. To quantify the difference between a mass bias distribution derived from actual SZE centers and its randomized counterpart, we define $\tau = \langle (M_{\text{biased}} -$

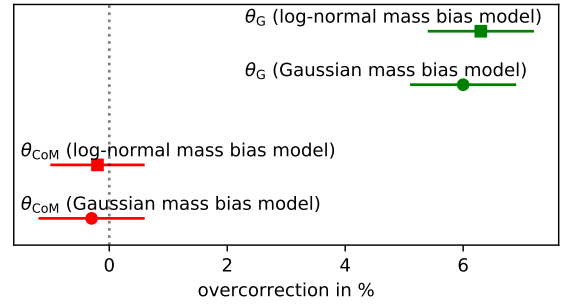


Figure 4. Overcorrection in percent, using different combinations of reference center and mass bias model.

$M_{\text{unbiased}})/M_{\text{unbiased}})$ as the expectancy value of the relative overcorrection induced by using random miscentering (a negative value of τ thus corresponds to an under-correction). Here, the subscript 'unbiased' refers only to the anisotropic miscentering.

3 RESULTS

We put the halos from the simulation through the mass fit with four different centering schemes for the reduced shear profile: (1) as a general reference, the gravitational center Θ_{G} ; (2) the SZE centers Θ_{SZE} as determined from the peak SZE signal; (3) SZE centers randomized from the empirical distribution of $|\Theta_{\text{SZE}} - \Theta_{\text{G}}|$; and (4) SZE centers randomized from the empirical distribution of $|\Theta_{\text{SZE}} - \Theta_{\text{CoM}}|$. The resulting estimates for the corresponding weak lensing mass distributions are summarized in Table 1. A graphical representation of the results is shown in Fig. 4.

With no miscentering with respect to the gravitational center, masses are underestimated by around 1% (row zero of Table 1). Taking the actual SZE centers results instead in an overestimation of 2% (row 3). We stress that these results are specific to the mass range, redshift and radial weights (in particular, the choice of r_{min} , r_{max} and the assumption of uniformly distributed background galaxies), as well as the choice of model (here, the NFW density profile in conjunction with the chosen concentration–mass relation).

With Θ_{G} as the reference, masses corrected by a mass bias distribution b , derived from the isotropic miscentering $|\Theta_{\text{SZE}} - \Theta_{\text{G}}|$, results in a mass overcorrection of $\sim 6\%$, independently of which dis-

	reference			log-normal distribution			normal distribution		
	center	mass	centering	μ_b	σ_b	τ	$\mu_{\log b}$	$\sigma_{\log b}$	τ
0	Θ_G	$M_{500,G}$	Θ_G	-0.024 ± 0.006	0.167 ± 0.004		0.991 ± 0.006	0.179 ± 0.004	
1	Θ_G	$M_{500,G}$	Θ_{CoM}	0.015 ± 0.006	0.167 ± 0.004		1.030 ± 0.007	0.191 ± 0.005	
2	Θ_G	$M_{500,G}$	$ \Theta_{\text{CoM}} - \Theta_G _{(r)}$	-0.051 ± 0.007	0.189 ± 0.005	0.068 ± 0.009	0.967 ± 0.007	0.187 ± 0.005	0.065 ± 0.010
3	Θ_G	$M_{500,G}$	Θ_{SZE}	0.005 ± 0.006	0.165 ± 0.004		1.020 ± 0.006	0.184 ± 0.005	
4	Θ_G	$M_{500,G}$	$ \Theta_{\text{SZE}} - \Theta_G _{(r)}$	-0.056 ± 0.007	0.187 ± 0.005	0.063 ± 0.009	0.962 ± 0.006	0.183 ± 0.005	0.060 ± 0.009
5	Θ_{CoM}	$M_{500,G}$	Θ_{SZE}	0.005 ± 0.006	0.165 ± 0.004		1.020 ± 0.006	0.184 ± 0.005	
6	Θ_{CoM}	$M_{500,G}$	$ \Theta_{\text{SZE}} - \Theta_{\text{CoM}} _{(r)}$	0.007 ± 0.006	0.169 ± 0.004	-0.002 ± 0.008	1.023 ± 0.007	0.190 ± 0.005	-0.003 ± 0.009
7	Θ_{CoM}	$M_{500,\text{CoM}}$	Θ_{SZE}	-0.034 ± 0.006	0.164 ± 0.004		0.981 ± 0.006	0.174 ± 0.004	
8	Θ_{CoM}	$M_{500,\text{CoM}}$	$ \Theta_{\text{SZE}} - \Theta_{\text{CoM}} _{(r)}$	-0.032 ± 0.006	0.167 ± 0.004	-0.002 ± 0.008	0.983 ± 0.006	0.178 ± 0.004	-0.003 ± 0.009

Table 1. Results of fitting log-normal and normal distributions to the mass bias b , given the reference center, reference mass and type of centering used. Rows are numbered 0 – 8. Pairs of rows separated by horizontal lines represent actual vs. randomized (odd and even row numbers, respectively) centerings. Rows 3 and 5 have identical mass bias distributions, as both are derived from actual SZE centers and have the same mass reference. In each even row (excepting row 0), the overcorrection τ , representing the mass overcorrection due to randomized miscentering (with respect to the row immediately above), is reported.

tribution is taken as a model (rows 3 and 4 of Table 1). This results is fully consistent with S+24. When we instead use the center of mass Θ_{CoM} as the reference center (rows 5–8), we find a mass overcorrection consistent with zero, with an uncertainty of around one percent. The statement is true whether the reference mass is $M_{500,G}$ (rows 5–6) or $M_{500,\text{CoM}}$ (rows 7–8); this is expected as the ratio of the two masses is a constant for each halo in the sample.

The aforementioned results suggest that systematic errors in the mass bias, resulting from the use of an isotropic miscentering distribution, are at or below one percent when the center of mass is taken as the "true" halo center.

For comparison, we also report the overcorrection in the case where the shear profiles are centered on Θ_{CoM} , with Θ_G as reference (rows 1 and 2 in the table). Here, the overcorrection is consistent with that derived taking the SZ centers, implying that most of the anisotropic mass bias originates in the difference between Θ_G and Θ_{CoM} , and that the center of mass is thus a more suitable proxy than the gravitational center for the peak of the surface mass density.

4 DISCUSSION

Considering the significant correlation between Θ_{SZE} and Θ_{CoM} , it is unsurprising that the overcorrection is reduced with Θ_{CoM} , rather than Θ_G , as the reference. While the absolute miscentering of the SZE peak with respect to the center of mass is reduced by about 50% on average, the overcorrection, attributed to a non-isotropic miscentering distribution, is reduced from 6% to $\pm 1\%$. To arrive at this result, we smoothed the SZE signal to a resolution of one arcminute. To see the effects of modifying this scale, we repeat the analysis with the SZE images smoothed to 0.5 arcminutes. While the result is fully consistent in terms of overcorrection, there is a slight broadening (around 6%) of the SZE miscentering distribution with respect to the center of mass, suggesting that more resolved SZE images would in fact be sub-optimal.

S+24 found very similar overcorrection factors from SZE peaks and X-ray centroids. Considering also that X-rays trace mass density of the intra-cluster gas, while the SZE traces gas pressure, we speculate that the center of mass may also serve as a more unbiased mass reference when X-ray centroids are used as the center proxy, although we have not shown this explicitly.

Our SZE peak miscentering distributions are artificially narrow, as

we have not included any noise in the SZE images. This, however, is of little consequence, as an isotropic broadening of the miscentering distribution would not be expected to cause anisotropic effects in the mass bias (see S+24 for a more in-depth discussion of this statement).

We suggest that a relatively simple solution to the problem of non-isotropic miscentering lies in moving the reference center of a halo to the center of mass. As a practical consequence, one would then need to recalculate miscentering distributions with respect to a suitably defined center of mass. A re-definition of the halo mass function, on the other hand, would not be required.

As an additional test, we repeat the analysis without re-calibrating M_{500} when finding the center of mass. Again, we find results fully consistent with those reported in the previous section. As the mass difference is small ($M_{500,\text{CoM}}$ is 5% higher than $M_{500,G}$ on average), this is unsurprising – the corresponding mean ratio of r_{500} is less than 2%.

5 SUMMARY AND CONCLUSIONS

Using a snapshot of the Magneticum simulations of massive halos at redshift $z = 0.7$, we derived miscentering distributions of the SZE peak in 1 arcminute convolved noiseless SZE images with respect to both the gravitational center and the center of mass. Randomizing both miscentering distributions to make them isotropic by construction, we compared the results to using the actual SZE peaks for each halo. The effect on the weak lensing mass bias, disregarding all other sources of bias, clearly favor the center of mass as the default center proxy, as there is no detectable difference (at the one percent level) in the mass bias whether the randomized or actual miscentering is used. Conversely, a mass overcorrection of approximately 6% is found when the gravitational center is taken as the center proxy, and an isotropic miscentering distribution is assumed. As a consequence, we suggest that the center of mass, rather than the bottom of the gravitational potential, represented in simulations by the most bound particle in a halo, may for practical reasons be a more robust marker of the halo center when estimating miscentering distributions from cosmological simulations, while the halo mass function needs not be modified. We speculate that a similar approach may be used when X-ray centroids are the center proxy of choice.

ACKNOWLEDGEMENTS

We would like to thank Klaus Dolag, Antonio Ragagnin, Alex Saro and Veronica Biffi for their help in using and interpreting the Magneticum Pathfinder simulations. We thank Peter Schneider for helpful discussions.

We acknowledge support from the German Federal Ministry for Economic Affairs and Energy (BMWi) provided through DLR under projects 50OR2002, 50OR2106, 50OR2302, and 50QE2002 as well as support provided by the Deutsche Forschungsgemeinschaft (DFG, German Research Foundation) under grant 415537506.

The Innsbruck authors acknowledge support provided by the Austrian Research Promotion Agency (FFG) and the Federal Ministry of the Republic of Austria for Climate Action, Environment, Mobility, Innovation and Technology (BMK) via the Austrian Space Applications Programme with grant numbers 899537, 900565, and 911971.

DATA AVAILABILITY

The data underlying this work will be shared on reasonable request to the corresponding author.

REFERENCES

- Allen S. W., Evrard A. E., Mantz A. B., 2011, *ARA&A*, **49**, 409
 Applegate D. E., et al., 2014, *MNRAS*, **439**, 48
 Applegate D. E., et al., 2016, *MNRAS*, **457**, 1522
 Bahé Y. M., McCarthy I. G., King L. J., 2012, *MNRAS*, **421**, 1073
 Bartelmann M., 1996, *A&A*, **313**, 697
 Becker M. R., Kravtsov A. V., 2011, *ApJ*, **740**, 25
 Bocquet S., et al., 2019, *ApJ*, **878**, 55
 Bocquet S., Heitmann K., Habib S., Lawrence E., Uram T., Frontiere N., Pope A., Finkel H., 2020, *ApJ*, **901**, 5
 Bocquet S., et al., 2023, *arXiv e-prints*, p. [arXiv:2310.12213](https://arxiv.org/abs/2310.12213)
 Bocquet S., et al., 2024, *arXiv e-prints*, p. [arXiv:2401.02075](https://arxiv.org/abs/2401.02075)
 Bond J. R., Cole S., Efstathiou G., Kaiser N., 1991, *ApJ*, **379**, 440
 Bullock J. S., Kolatt T. S., Sigad Y., Somerville R. S., Kravtsov A. V., Klypin A. A., Primack J. R., Dekel A., 2001, *MNRAS*, **321**, 559
 Child H. L., Habib S., Heitmann K., Frontiere N., Finkel H., Pope A., Morozov V., 2018, *ApJ*, **859**, 55
 Chiu I. N., Klein M., Mohr J., Bocquet S., 2023, *MNRAS*,
 Diemer B., Joyce M., 2019, *ApJ*, **871**, 168
 Diemer B., Kravtsov A. V., 2015, *ApJ*, **799**, 108
 Dietrich J. P., et al., 2019, *MNRAS*, **483**, 2871
 Dolag K., Stasyszyn F., 2009, *MNRAS*, **398**, 1678
 Dolag K., Jubelgas M., Springel V., Borgani S., Rasia E., 2004, *ApJ*, **606**, L97
 Dolag K., Hansen F. K., Roncarelli M., Moscardini L., 2005a, *MNRAS*, **363**, 29
 Dolag K., Vazza F., Brunetti G., Tormen G., 2005b, *MNRAS*, **364**, 753
 Dolag K., Komatsu E., Sunyaev R., 2016, *MNRAS*, **463**, 1797
 Fabjan D., Borgani S., Tornatore L., Saro A., Murante G., Dolag K., 2010, *MNRAS*, **401**, 1670
 Ghirardini V., et al., 2024, *arXiv e-prints*, p. [arXiv:2402.08458](https://arxiv.org/abs/2402.08458)
 Grandis S., Mohr J. J., Dietrich J. P., Bocquet S., Saro A., Klein M., Paulus M., Capasso R., 2019, *MNRAS*, **488**, 2041
 Grandis S., Bocquet S., Mohr J. J., Klein M., Dolag K., 2021, *MNRAS*, **507**, 5671
 Grandis S., et al., 2024, *A&A*, **687**, A178
 Gupta N., Saro A., Mohr J. J., Dolag K., Liu J., 2017, *MNRAS*, **469**, 3069
 Haiman Z., Mohr J. J., Holder G. P., 2001, *ApJ*, **553**, 545
 Heitmann K., Higdon D., Nakhleh C., Habib S., 2006, *ApJ*, **646**, L1
 Henson M. A., Barnes D. J., Kay S. T., McCarthy I. G., Schaye J., 2017, *MNRAS*, **465**, 3361
 Hirschmann M., Dolag K., Saro A., Bachmann L., Borgani S., Burkert A., 2014, *MNRAS*, **442**, 2304
 Hoekstra H., Hartlap J., Hilbert S., van Uitert E., 2011, *MNRAS*, **412**, 2095
 Jenkins A., Frenk C. S., White S. D. M., Colberg J. M., Cole S., Evrard A. E., Couchman H. M. P., Yoshida N., 2001, *MNRAS*, **321**, 372
 Kaiser N., Squires G., Broadhurst T., 1995, *ApJ*, **449**, 460
 Kilbinger M., 2015, *Reports on Progress in Physics*, **78**, 086901
 Kleinebreil F., et al., 2024, *arXiv e-prints*, p. [arXiv:2402.08456](https://arxiv.org/abs/2402.08456)
 Klypin A., Yepes G., Gottlöber S., Prada F., Heß S., 2016, *MNRAS*, **457**, 4340
 Komatsu E., et al., 2011, *ApJS*, **192**, 18
 Lee B. E., Le Brun A. M. C., Haq M. E., Deering N. J., King L. J., Applegate D., McCarthy I. G., 2018, *MNRAS*, **479**, 890
 Mandelbaum R., Tasitsiomi A., Seljak U., Kravtsov A. V., Wechsler R. H., 2005, *MNRAS*, **362**, 1451
 Mantz A. B., Allen S. W., Morris R. G., Rapetti D. A., Applegate D. E., Kelly P. L., von der Linden A., Schmidt R. W., 2014, *MNRAS*, **440**, 2077
 McClintock T., et al., 2019, *MNRAS*, **482**, 1352
 Meneghetti M., et al., 2014, *ApJ*, **797**, 34
 Navarro J. F., Frenk C. S., White S. D. M., 1997, *ApJ*, **490**, 493
 Oguri M., Hamana T., 2011, *MNRAS*, **414**, 1851
 Planck Collaboration et al., 2016, *A&A*, **594**, A24
 Prada F., Klypin A. A., Cuesta A. J., Betancort-Rijo J. E., Primack J., 2012, *MNRAS*, **423**, 3018
 Press W. H., Schechter P., 1974, *ApJ*, **187**, 425
 Ragagnin A., Dolag K., Biffi V., Cadolle Bel M., Hammer N. J., Krukau A., Petkova M., Steinborn D., 2017, *Astronomy and Computing*, **20**, 52
 Schrabback T., et al., 2018, *MNRAS*, **474**, 2635
 Schrabback T., et al., 2021, *MNRAS*, **505**, 3923
 Seitz C., Schneider P., 1997, *A&A*, **318**, 687
 Seljak U., 2000, *MNRAS*, **318**, 203
 Sheth R. K., Tormen G., 1999, *MNRAS*, **308**, 119
 Sommer M. W., Schrabback T., Applegate D. E., Hilbert S., Ansarinejad B., Floyd B., Grandis S., 2022, *MNRAS*, **509**, 1127
 Sommer M. W., Schrabback T., Ragagnin A., Rockenfeller R., 2024, *MNRAS*, **532**, 3359
 Springel V., 2005, *MNRAS*, **364**, 1105
 Springel V., Hernquist L., 2003, *MNRAS*, **339**, 312
 Springel V., White M., Hernquist L., 2001, *ApJ*, **549**, 681
 Springel V., Di Matteo T., Hernquist L., 2005a, *MNRAS*, **361**, 776
 Springel V., et al., 2005b, *Nature*, **435**, 629
 Sunyaev R. A., Zeldovich Y. B., 1970, *Comments on Astrophysics and Space Physics*, **2**, 66
 Sunyaev R. A., Zeldovich I. B., 1980, *ARA&A*, **18**, 537
 Teklu A. F., Remus R.-S., Dolag K., Beck A. M., Burkert A., Schmidt A. S., Schulze F., Steinborn L. K., 2015, *ApJ*, **812**, 29
 Tollet E., et al., 2016, *MNRAS*, **456**, 3542
 Tornatore L., Borgani S., Dolag K., Matteucci F., 2007, *MNRAS*, **382**, 1050
 Wiersma R. P. C., Schaye J., Theuns T., Dalla Vecchia C., Tornatore L., 2009, *MNRAS*, **399**, 574
 Wright C. O., Brainerd T. G., 2000, *ApJ*, **534**, 34
 Zohren H., et al., 2022, *A&A*, **668**, A18

This paper has been typeset from a $\text{\TeX}/\text{\LaTeX}$ file prepared by the author.